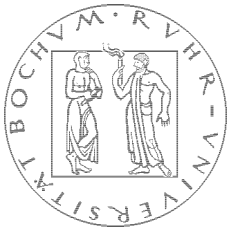

Ruhr University Bochum
Lehrstuhl für Technische Mechanik

Preprint 02-2005

On the efficient implementation of an elastoplastic damage model for large-scale analyses of material failure: A multiscale approach

J. Mosler

This is a preprint of an article published in:

Computers & Structures, Vol. 83, Issues 4–5, 369–382

(2005)

On the efficient implementation of an elastoplastic damage model for large-scale analyses of material failure: A multiscale approach

J. Mosler

Lehrstuhl für Technische Mechanik
Ruhr University Bochum
Universitätsstr. 150,D-44780 Bochum, Germany
E-Mail: mosler@tm.bi.ruhr-uni-bochum.de
URL: www.tm.bi.ruhr-uni-bochum.de/mosler

SUMMARY

This paper is concerned with an efficient implementation of material models suitable for the analyses of large-scale engineering problems. Based on the enhanced assumed strain concept (EAS), the final failure kinematics of solids associated with a small-scale are incorporated into the large-scale phenomenological macroscopic constitutive equations. To model the structural response realistically both plastic strains as well as damage-induced stiffness degradation are taken into account. In contrast to the original EAS concept, the parameters defining the enhanced strains are condensed out at the material level. The presented constitutive and numerical framework is applicable to a broad range of different localization phenomena including mode-I, mode-II and mixed-mode material failure. The applicability and the performance of the proposed finite element formulation is investigated by means of a re-analysis of a two-dimensional L-shaped slab as well as by means of a three-dimensional ultimate load analysis of a notched concrete beam subjected to an eccentric load.

1 Introduction

Numerical analyses of large-scale engineering structures undergoing fracture processes such as cracking in brittle materials or the development of shear bands in soils still represent a challenge to the scientific community. The complexity associated with those problems results, at least, from two reasons (see [1]).

Firstly, fracture processes often involve strain localization. This leads to the loss of ellipticity [2, 3] of the governing equations (in the static case) and consequently, to the well-known pathological mesh dependence of the numerically computed results [4, 5]. In the limiting case (the characteristical diameter of the finite element discretization converges to zero), material failure without any dissipation appears. Hence, different enhanced models which overcome the disability of classical (local) continuum theories mentioned have been proposed in the recent decade, see, e.g. References [6–11]. Each of these models makes use of an internal length parameter related to the specific material. This length scale is associated with the width of the localization zone. By this means, the width of the failure zone is postulated explicitly and, consequently, does not depend on the spatial discretization.

The second problem concerned with the numerical modeling of large-scale engineering structures undergoing fracture processes results from a different length scale of the analyzed

structure compared to the width of the bands showing localized deformations. In typical applications, the length corresponding to the small-scale varies from a couple of millimeters (e.g. shear bands occurring in metals [12, 13]) up to more than one kilometer (e.g. in geotechnical problems) whereas the characteristical diameter of the structure is several dimensions larger. Applying enhanced continuum models such as nonlocal theories, gradient-enhanced approaches or COSSERAT continua to the numerical analyses of those problems, a sufficiently fine resolution of the localization zone with at least two to three rows of elements to guarantee mesh objectivity is required. Hence, computational cost may be prohibitive even if adaptive techniques are used.

As a result of the mesh dependence of standard local continuum models and the required numerical cost associated with the mentioned enhanced continuum theories, alternative methods accounting for the multiscale character of the underlying physical problem have been proposed. Most of these models are characterized by the incorporation of the small-scale kinematics into a large-scale phenomenological macroscopic material model, see, e.g. References [14–22]. In these works, small-scale kinematics are captured by an enriched displacement field or a strain field, respectively. Following [14, 23, 24], the proposed multiscale material model is based on the so-called strong discontinuity approach (SDA). In this concept, the failure zone is represented as a surface of discontinuous displacements within the respective finite elements. More precisely and in accordance with the underlying enhanced assumed strain (EAS) concept, only the (enhanced) strains resulting from the discontinuous displacement field appear explicitly in the formulation.

The enhanced strains associated with the displacement jump are related to their conjugated stresses by additional constitutive equations. In contrast to classical continuum mechanics, these equations are characterized by a traction-separation law [14] (instead of a stress-strain relationship). For the development of such laws, two different concepts can be applied. According to [14, 25–27], the projection of a stress-strain law onto a material surface leads to the mentioned interface law. Alternatively, the constitutive equations corresponding to the discontinuous displacement field can be postulated independently [27–31]. Analogously to classical continuum mechanics, the traction-separation laws can be subdivided into plasticity-based [24, 32, 33] and damage-based models [14, 25, 34]. Recently, a coupled elastoplastic anisotropic damage interface law for the modeling of cracking in brittle structures has been proposed in [35]. In this Reference, an additive split of the compliance tensor (according to [36, 37]), together with a yield function of the form $\phi = (\boldsymbol{N} \otimes \boldsymbol{M}) : \boldsymbol{\sigma} - q$, has been assumed ($\boldsymbol{\sigma}$, $\boldsymbol{N}$, $\boldsymbol{M}$, q denote the stress tensor $\boldsymbol{\sigma}$, two unit vectors defining the normal $\boldsymbol{N}$ of the failure surface and the direction $\boldsymbol{M}$ of the displacement discontinuity, and a stress-like internal variable q, respectively). On the one hand, the considered yield function restricts the range of applications of the model considerably. On the other hand, the memory requirements of the numerical implementation resulting from the anisotropic damage evolution are very high.

In this paper, we present an elastoplastic isotropic damage model not restricted to any particular material. Referring to the yield function and the evolution equations, no special assumption has to be made. That is, in contrast to previous works, the numerical model suggested can be applied to the analysis of a broad range of different physical phenomena such as cracking in brittle structures or the formation of shear bands in soils. Furthermore, the model accounts for two very important physical effects, namely plastic deformations as well as stiffness degradation. By this means, the application range of the finite element formulation presented is further increased. The proposed class of constitutive interface laws is incorporated into a three-dimensional finite element formulation. The suggested implementation, similar to [26], is restricted to the material level and formally identical to the classical return-mapping algorithm [38, 39]. As a consequence, the framework of computational plasticity can be applied. More precisely, and

in contrast to previous works, subroutines designed for standard (continuous) plasticity models can be used. Only minor modifications of theses subroutines are required. As a consequence, the costs associated with the numerical implementation can be reduced to a minimum. Furthermore, the finite element formulation shows the well known characteristics of the return-mapping algorithm. That is, the algorithm is numerically very robust and efficient.

This paper is organized as follows: Section 2 is concerned with a short summary of the basic kinematic assumptions on the small-scale. The development of the constitutive equations governing the discontinuous part of the displacement field is addressed in Section 3. In Section 4, an efficient implementation of the presented multiscale material model is proposed. The applicability and the performance of the resulting finite element formulation is investigated by means of a re-analysis of a two-dimensional L-shaped slab (Subsection 5.2) as well as by means of a three-dimensional ultimate load analysis of a notched concrete beam subjected to an eccentric load (Subsection 5.1).

2 Kinematics associated with the small-scale

In this section, a short summary of the kinematics associated with the small-scale is given. These kinematics are characterized by highly localized deformations resulting from the formation of cracks or shear bands, respectively. From a macroscopic point of view, the small-scale displacement field can be approximated by discontinuous deformation mappings. These mappings are presented in this section. For further details, refer to [14, 24, 25, 27, 31, 35].

In what follows, $\Omega \subset \mathbb{R}^3$ is an open bounded set, $\boldsymbol{X}_0 \in \Omega$ a (fixed) point and $\partial_{\mathrm{s}}\Omega \subset \Omega$ represents a $\mathcal{C}^\infty$ hyperplane (see Figure 1). This surface with normal vector field $\boldsymbol{N}$ is assumed

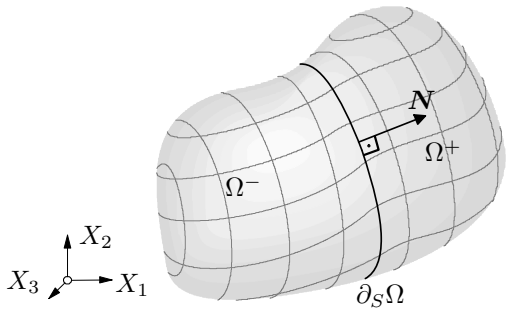

Figure 1: Body $\Omega \subset \mathbb{R}^3$ separated into two parts Ω^- and Ω^+ by a two-dimensional sub manifold $\partial_{\mathrm{s}}\Omega$ of class $\mathcal{C}^1$.

to separate the body Ω into the disjunct subsets Ω^- and Ω^+. If the displacements are smooth and bounded in Ω^- and Ω^+, the discontinuity of the mapping $\boldsymbol{u}$ at $\boldsymbol{X}_0 \in \partial_{\mathrm{s}}\Omega$

$$[\![\boldsymbol{u}(\boldsymbol{X}_0)]\!] := \boldsymbol{u}^+(\boldsymbol{X}_0) - \boldsymbol{u}^-(\boldsymbol{X}_0) \quad \forall \boldsymbol{X}_0 \in \partial_{\mathrm{s}}\Omega, \tag{1}$$

is well defined. In Equation (1), $\boldsymbol{u}^+(\boldsymbol{X}_0)$ and $\boldsymbol{u}^-(\boldsymbol{X}_0)$ denote the right hand limit and the left hand limit of $\boldsymbol{u}$ in $\boldsymbol{X}_0$. From a physical point of view, this discontinuity may represent deformations induced by crack opening of shear sliding displacements. In what follows, a displacement field of the format

$$\boldsymbol{u} = \underbrace{\bar{\boldsymbol{u}}}_{\text{large-scale}} + \underbrace{[\![\boldsymbol{u}]\!]\ (H_{\mathrm{s}} - \varphi)}_{\text{small-scale}}, \quad \text{with} \quad \bar{\boldsymbol{u}} \in \mathcal{C}^\infty(\Omega, \mathbb{R}^3),\ \varphi \in \mathcal{C}^\infty(\Omega, \mathbb{R}). \tag{2}$$

is adopted (see [24]). In Equation (2), $H_{\mathrm{s}} : \Omega \rightarrow \{0;1\}$ denotes the HEAVISIDE function with respect to $\partial_{\mathrm{s}}\Omega$. Clearly, $\boldsymbol{u}$ belongs to the space of bounded deformations as introduced in [40, 41] (see also [31]). According to Equation (2), the small-scale field is able to capture highly localized deformations. This field depends on the smooth ramp function φ which allows to prescribe the boundary conditions in terms of $\bar{\boldsymbol{u}}$ (see [25]). Referring to the finite element method and following References [24, 27], φ is designed by the standard interpolation functions N_i associated with node i as

$$\varphi = \sum_{i=1}^{n_{\overline{\Omega^+}}} N_i. \tag{3}$$

Here and henceforth, the notation $\sum_{i=1}^{n_{\overline{\Omega^+}}}$ means the summation over all nodes of the respective localized finite element belonging to the closure of Ω^+ denoted as $\overline{\Omega^+}$. That is, φ is computed separately for each element undergoing localization. Applying the generalized derivative D to the Heaviside function, the identity

$$DH_{\mathrm{s}} = \boldsymbol{N}\ \delta_{\mathrm{s}} \tag{4}$$

is derived in the sense of distributions (see [42]). In Equation (4), δ_{s} represents the DIRAC-delta distribution with respect to $\partial_{\mathrm{s}}\Omega$. From Equations (2) and (4) the linearized strain tensor is obtained as

$$\boldsymbol{\varepsilon} := \boldsymbol{\nabla}^{\mathrm{sym}}\bar{\boldsymbol{u}} \underbrace{-(\llbracket \boldsymbol{u} \rrbracket \otimes \boldsymbol{\nabla}\varphi)^{\mathrm{sym}} + (\llbracket \boldsymbol{u} \rrbracket \otimes \boldsymbol{N})^{\mathrm{sym}}\ \delta_{\mathrm{s}} + \boldsymbol{\nabla}\llbracket \boldsymbol{u} \rrbracket\ (H_{\mathrm{s}} - \varphi)}_{\text{small-scale}}. \tag{5}$$

In what follows, the macroscopic strain field $\boldsymbol{\varepsilon}_{\mathrm{M}} := \boldsymbol{\nabla}^{\mathrm{sym}}\bar{\boldsymbol{u}}$ is enriched with the enhanced strain $\boldsymbol{\varepsilon}_{\mathrm{s}}$ associated with the small-scale. Neglecting the gradient of the displacement discontinuity, i.e. $\boldsymbol{\nabla}\llbracket \boldsymbol{u} \rrbracket = \boldsymbol{0}$, these strains are assumed as

$$\boldsymbol{\varepsilon}_{\mathrm{s}} := -\underbrace{(\llbracket \boldsymbol{u} \rrbracket \otimes \boldsymbol{\nabla}\varphi)^{\mathrm{sym}}}_{:=\,\tilde{\boldsymbol{\varepsilon}}} + (\llbracket \boldsymbol{u} \rrbracket \otimes \boldsymbol{N})^{\mathrm{sym}}\ \delta_{\mathrm{s}}. \tag{6}$$

Consequently, the resulting strain field

$$\boldsymbol{\varepsilon} = \boldsymbol{\varepsilon}_{\mathrm{M}} + \boldsymbol{\varepsilon}_{\mathrm{s}} \tag{7}$$

is adopted. Since the presented finite element formulation is based on the enhanced assumed strain (EAS) concept [43], the enhanced strain field (6) represents a suitable choice.

3 Constitutive law associated with the small-scale

The development of the constitutive equations associated with the small-scale is addressed in this section. As will be shown and in contrast to classical continuum mechanics, the material law governing the behavior of the small-scale is not characterized by a stress-strain relationship.

3.1 Fundamentals

Here and henceforth, inelastic deformations induced by plasticity or material damage are assumed to be restricted to $\partial_{\mathrm{s}}\Omega$, while the remaining part of the body $\Omega/\partial_{\mathrm{s}}\Omega$ unloads elastically [24]. As a consequence, the stresses $\boldsymbol{\sigma}$ in $\Omega^{\pm}$ are computed from HOOKE's law, i.e. $\boldsymbol{\sigma} = \mathbb{C} : \boldsymbol{\varepsilon}$.

Next, the constitutive equations corresponding to points $\boldsymbol{X} \in \partial_{\mathrm{s}}\Omega$ are developed. According to the extension of the principle of virtual work to domains exhibiting singular surfaces $\partial_{\mathrm{s}}\Omega$, the traction vector $\boldsymbol{t} := \boldsymbol{\sigma} \cdot \boldsymbol{N}$ acting on $\partial_{\mathrm{s}}\Omega$ is conjugated to the displacement jump $[\![\boldsymbol{u}]\!]$ (see [24, 27]). Hence, a material law of the type

$$\boldsymbol{t}_{\mathrm{s}} = \boldsymbol{t}_{\mathrm{s}}([\![\boldsymbol{u}]\!]), \quad \text{with} \quad \boldsymbol{t}_{\mathrm{s}} := \boldsymbol{t}|_{\partial_{\mathrm{s}}\Omega} \tag{8}$$

represents an admissible choice (see [24, 35]). Assuming traction continuity across $\partial_{\mathrm{s}}\Omega$, i.e.

$$\boldsymbol{t}^{\pm}(\boldsymbol{X}_0) = \boldsymbol{t}(\boldsymbol{X}_0) \quad \forall \boldsymbol{X}_0 \in \partial_{\mathrm{s}}\Omega, \tag{9}$$

Equation (8) yields [27, 31]

$$\boldsymbol{t}^{+} = \boldsymbol{t}_{\mathrm{s}}([\![\boldsymbol{u}]\!]) \quad \forall \boldsymbol{X}_0 \in \partial_{\mathrm{s}}\Omega. \tag{10}$$

In what follows, a traction-separation law, i.e. $\boldsymbol{t}^{+} = \boldsymbol{t}_{\mathrm{s}}([\![\boldsymbol{u}]\!])$, is derived from a singularly distributed stored energy functional Ψ (see e.g. [16, 25, 27, 31]). Similarly to [16, 24, 25, 27, 35], an additive split of the stored energy Ψ into a regularly distributed part Ψ_{reg} and a singular part Ψ_{in} leading to

$$\Psi = \Psi_{\mathrm{reg}} + \Psi_{\mathrm{in}}\, \delta_{\mathrm{s}} \tag{11}$$

is assumed. Postulating $[\![\boldsymbol{u}]\!]$ to be associated only with inelastic deformations, Ψ_{in} is specified by $\Psi_{\mathrm{in}} = \Psi_{\mathrm{in}}(\boldsymbol{\alpha}([\![\boldsymbol{u}]\!]))$ in terms of the displacement-like internal variable $\boldsymbol{\alpha} \in \mathbb{R}^n$ depending on the displacement discontinuity. Similarly to standard plasticity [38], the space of admissible stresses

$$\mathbb{E}_{\boldsymbol{t}} := \left\{(\boldsymbol{t}, \boldsymbol{q}) \in \mathbb{R}^3 \times \mathbb{R}^n \mid \phi(\boldsymbol{t}, \boldsymbol{q}) \leq 0\right\} \quad \forall \boldsymbol{X} \in \partial_{\mathrm{s}}\Omega \tag{12}$$

is defined by means of a yield (failure) function $\phi(\boldsymbol{t}, \boldsymbol{q})$, which depends on the traction vector $\boldsymbol{t}$ and a vector of stress-like hardening/softening parameters $\boldsymbol{q} = \boldsymbol{q}(\boldsymbol{\alpha})$ conjugated to $\boldsymbol{\alpha}$. Note that Definition (12) includes isotropic hardening/softening as well as the kinematical counterpart (see [27, 31]). For instance, the yield criterion

$$\begin{aligned} q = ||\boldsymbol{t}_{\mathrm{s}}|| \quad \text{and} \quad \phi : \mathbb{R}^3 \times \mathbb{R}_+ &\rightarrow \mathbb{R} \\ (\boldsymbol{t}, q) &\mapsto ||\boldsymbol{t}|| - q, \end{aligned} \tag{13}$$

represents a suitable choice. In Equation (13), $||\bullet|| : \mathbb{R}^3 \rightarrow \mathbb{R}_+$ denotes a norm, e.g., the EUCLIDEAN norm.

The material law is completed by the evolution equations associated with the inelastic deformations, i.e. $[\![\boldsymbol{u}]\!]$ and the internal displacement-like variables $\boldsymbol{\alpha}$. Introducing two potentials $g(\boldsymbol{t}, \boldsymbol{q}), h(\boldsymbol{t}, \boldsymbol{q})$, the rates of $[\![\boldsymbol{u}]\!]$ and $\boldsymbol{\alpha}$ are postulated as

$$[\![\dot{\boldsymbol{u}}]\!] := \lambda\, \partial_{\boldsymbol{t}} g \quad \text{and} \quad \dot{\boldsymbol{\alpha}} := \lambda\, \partial_{\boldsymbol{q}} h \quad \text{with} \quad \partial_{\boldsymbol{t}} g := \frac{\partial g}{\partial \boldsymbol{t}}. \tag{14}$$

Here and henceforth, the superposed dot is used to represent the time derivative. Analogously to standard plasticity, the plastic multiplier λ is computed from the consistency condition $\dot{\phi} = 0$. For the special choice $g = \phi$ and $h = \phi$, associative evolution equations are obtained. In this case, the rates (14) are derived from the principle of maximum dissipation (see [27, 31]).

So far, only loading, i.e. $\lambda > 0$, has been considered. Now, the unloading behavior is specified. According to [44], an additive decomposition of the inelastic deformations into plasticity and damage-induced effects is assumed. Adopting this idea to the proposed model, the rate of the displacement jump is postulated as

$$[\![\dot{\boldsymbol{u}}]\!] =: [\![\dot{\boldsymbol{u}}]\!]^{\mathrm{pl}} + [\![\dot{\boldsymbol{u}}]\!]^{\mathrm{dam}}. \tag{15}$$

Following [44], a scalar coupling parameter $\beta \in [0;1]$ is introduced via

$$[\![\dot{\boldsymbol{u}}]\!]^{\mathrm{pl}} = (1-\beta)\ [\![\dot{\boldsymbol{u}}]\!]\,, \qquad [\![\dot{\boldsymbol{u}}]\!]^{\mathrm{dam}} = \beta\ [\![\dot{\boldsymbol{u}}]\!]\,. \tag{16}$$

As implied by Equations (16), for $\beta = 0.0$ a plasticity model is obtained, i.e. $[\![\dot{\boldsymbol{u}}]\!] = [\![\dot{\boldsymbol{u}}]\!]^{\mathrm{pl}}$, while $\beta = 1.0$ is associated with damage theory, i.e. $[\![\dot{\boldsymbol{u}}]\!] = [\![\dot{\boldsymbol{u}}]\!]^{\mathrm{dam}}$. Inserting Equations (16) into Equation (6) leads to

$$\dot{\tilde{\boldsymbol{\varepsilon}}} = \dot{\tilde{\boldsymbol{\varepsilon}}}^{\mathrm{pl}} + \dot{\tilde{\boldsymbol{\varepsilon}}}^{\mathrm{dam}}, \tag{17}$$

with

$$\dot{\tilde{\boldsymbol{\varepsilon}}}^{\mathrm{pl}} := (1-\beta)\ ([\![\dot{\boldsymbol{u}}]\!] \otimes \boldsymbol{\nabla}\varphi)^{\mathrm{sym}} \quad \text{and} \quad \dot{\tilde{\boldsymbol{\varepsilon}}}^{\mathrm{dam}} := \beta\ ([\![\dot{\boldsymbol{u}}]\!] \otimes \boldsymbol{\nabla}\varphi)^{\mathrm{sym}}\,. \tag{18}$$

As shown, assumptions (15) and (16) yields an unique decomposition of inelastic deformations into plasticity and damage-induced effects. However, in contrast to plasticity, damage evolution results in a change of the elastic behavior of the respective material. Consequently, a coupling of $[\![\boldsymbol{u}]\!]^{\mathrm{dam}}$, resp. $\tilde{\boldsymbol{\varepsilon}}^{\mathrm{dam}}$, to the 4-th order constitutive tensor $\mathbb{C}$ is required. Following [44], the compliance tensor $\mathbb{D} := \mathbb{C}^{-1}$ is coupled to the inelastic strains via

$$\dot{\mathbb{D}} : \boldsymbol{\sigma} = \dot{\boldsymbol{\varepsilon}}^{\mathrm{dam}} = \dot{\tilde{\boldsymbol{\varepsilon}}}^{\mathrm{dam}}. \tag{19}$$

In [44], Equation (19) has been derived from a free energy functional

$$\Psi(\mathbb{C}, \boldsymbol{\varepsilon}^{\mathrm{e}}, \alpha) = \frac{1}{2}\boldsymbol{\varepsilon}^{\mathrm{e}} : \mathbb{C} : \boldsymbol{\varepsilon}^{\mathrm{e}} - \Psi_{\mathrm{in}}(\alpha) \tag{20}$$

using the principle of maximum dissipation, together with a yield function of the type

$$\phi = \sigma_{\mathrm{eq}}(\boldsymbol{\sigma}) - \sigma_{\mathrm{f}} + q(\alpha), \tag{21}$$

where $\mathbb{C}$, $\boldsymbol{\varepsilon}^{\mathrm{e}}$, α, σ_{eq} and σ_{f} represent the elastic stiffness tensor associated with the damaged material, elastic strains, an internal strain like variable conjugated to the stress like variable q, a homogeneous function of degree one defining the yield (failure) surface and the failure strength of the undamaged material, respectively. Although the proposed traction-separation law is not restricted to the principle of maximum dissipation, resulting not necessarily in an associative flow rule (and evolution equations), Equation (19) is postulated. However and in contrast to [44], damage evolution is assumed to be isotropic, i.e.

$$\dot{\mathbb{D}} = \dot{\overline{\psi^{-1}}}\ \mathbb{D}_0, \tag{22}$$

where ψ denotes the so-called continuity and $\mathbb{D}_0$ represents the initial compliance tensor. Inserting Equation (22) and $(18)_2$ into Equation (19) yields

$$\begin{aligned} \dot{\overline{\psi^{-1}}}\ \mathbb{D}_0 : \boldsymbol{\sigma} &= \beta\ ([\![\dot{\boldsymbol{u}}]\!] \otimes \boldsymbol{\nabla}\varphi)^{\mathrm{sym}} \\ \Longleftrightarrow \qquad \dot{\overline{\psi^{-1}}}\ \boldsymbol{\sigma} &= \beta\ \mathbb{C}_0 : ([\![\dot{\boldsymbol{u}}]\!] \otimes \boldsymbol{\nabla}\varphi) \\ \Longrightarrow \qquad \dot{\overline{\psi^{-1}}} &= \beta\ \frac{\partial_{\boldsymbol{\sigma}}\phi : \mathbb{C}_0 : ([\![\dot{\boldsymbol{u}}]\!] \otimes \boldsymbol{\nabla}\varphi)}{\partial_{\boldsymbol{\sigma}}\phi : \boldsymbol{\sigma}}. \end{aligned} \tag{23}$$

In Equation (23), the equivalence $\mathbb{C}_0 : ([\![\dot{\boldsymbol{u}}]\!] \otimes \boldsymbol{\nabla}\varphi)^{\mathrm{sym}} = \mathbb{C}_0 : ([\![\dot{\boldsymbol{u}}]\!] \otimes \boldsymbol{\nabla}\varphi)$ following from the symmetry properties of $\mathbb{C}_0$ has been used. Since the identity $\partial_{\boldsymbol{\sigma}}\phi : \boldsymbol{A} = \partial_{\boldsymbol{t}}\phi \cdot \frac{\partial \boldsymbol{t}}{\partial \boldsymbol{\sigma}} : \boldsymbol{A}$ holds resulting in $\partial_{\boldsymbol{\sigma}}\phi = (\partial_{\boldsymbol{t}}\phi \otimes \boldsymbol{N})^{\mathrm{sym}}$, Equation (23) is rewritten as

$$\dot{\overline{\psi^{-1}}} = \beta\ \frac{(\partial_{\boldsymbol{t}}\phi \otimes \boldsymbol{N}) : \mathbb{C}_0 : ([\![\dot{\boldsymbol{u}}]\!] \otimes \boldsymbol{\nabla}\varphi)}{(\partial_{\boldsymbol{t}}\phi \otimes \boldsymbol{N}) : \boldsymbol{\sigma}}. \tag{24}$$

Alternatively, evolution Equation (23) can be interpreted as the projection of an anisotropic fourth-oder compliance tensor denoted as $\mathbb{D}^{\text{aniso}}$ onto the elastic constitutive tensor associated with the virgin material, i.e.

$$\dot{\overline{\psi^{-1}}} = \beta \, \frac{([\![\dot{\boldsymbol{u}}]\!] \otimes \boldsymbol{\nabla}\varphi) \otimes (\partial_{\boldsymbol{t}}\phi \otimes \boldsymbol{N})}{(\partial_{\boldsymbol{t}}\phi \otimes \boldsymbol{N}) : \boldsymbol{\sigma}} :: \mathbb{C}_0 = \mathbb{D}^{\text{aniso}} :: \mathbb{C}_0. \tag{25}$$

For the special choice $\phi = (\boldsymbol{m}\cdot\boldsymbol{t}) - q(\alpha([\![\boldsymbol{u}]\!]))$, together with associative evolution equations, the anisotropic damage tensor $\mathbb{D}^{\text{aniso}}$ has been derived in [35]. In the reference cited, $\boldsymbol{m}$ denotes the vector defining the direction of the rate of the displacement jump. For the analysis of cracking in brittle structures, $\boldsymbol{m}$ coincides with the direction of the maximum principle stress.

3.2 Dissipation predicted by the model

In what follows, it is shown that the proposed elastoplastic damage model yields a positive dissipation. Since for purely plastic models, a proof is contained in [14, 25], attention is restricted to $\beta = 1.0$, i.e. purely damage-induced dissipation. Hence, we want to show that ψ^{-1} represents a monotonically increasing function (in time), i.e. $\dot{\overline{\psi^{-1}}} \geq 0$. Clearly, it is possible to develop evolution equations which violate the second law of thermodynamics leading to $\dot{\overline{\psi^{-1}}} < 0$. As a consequence, reasonable assumptions governing the evolution equations have to be made. Here, we postulate associative evolution equations, i.e. $\partial_{\boldsymbol{t}}\phi =: \boldsymbol{m}$ and $[\![\dot{\boldsymbol{u}}]\!] = \lambda \, \boldsymbol{m}$. It should be noted that $\boldsymbol{m}$ may be time dependent. Inserting these assumptions into Equation (24) and setting $\beta = 1.0$, the rate of ψ^{-1} is computed as

$$\dot{\overline{\psi^{-1}}} = \lambda \, \frac{(\boldsymbol{N} \otimes \boldsymbol{m}) : \mathbb{C}_0 : (\boldsymbol{m} \otimes \boldsymbol{\nabla}\varphi)}{\boldsymbol{m} \cdot \boldsymbol{t}}. \tag{26}$$

The second assumption we make is that the denominator of Equation (26) is positive, i.e. $\boldsymbol{m}\cdot\boldsymbol{t} = \partial_{\boldsymbol{t}}\phi \cdot \boldsymbol{t} > 0$. This inequality is fulfilled for a broad range of different models. For instance, a yield function of the type

$$\phi = t_{\text{eq}}(\boldsymbol{t}) - q(\alpha([\![\boldsymbol{u}]\!])), \quad \text{with} \quad \partial_{\boldsymbol{t}}\phi \cdot \boldsymbol{t} = t_{\text{eq}} \tag{27}$$

leads to $\boldsymbol{m} \cdot \boldsymbol{t} = q(\alpha([\![\boldsymbol{u}]\!])) > 0$ (for loading, i.e. $\phi = 0$). Applying this inequality, together with $\lambda \geq 0$, to Equation (26), we obtain the identity

$$\dot{\overline{\psi^{-1}}} \geq 0 \quad \Longleftrightarrow \quad (\boldsymbol{N} \otimes \boldsymbol{m}) : \mathbb{C}_0 : (\boldsymbol{m} \otimes \boldsymbol{\nabla}\varphi) \geq 0. \tag{28}$$

Clearly, for the special case $\boldsymbol{\nabla}\varphi = \boldsymbol{N}$, Inequality $(28)_2$ represents the strong ellipticity condition which is fulfilled for HOOKE's law [2, 3]. Additionally, for RANKINE type models characterized by $\boldsymbol{N} = \boldsymbol{m}$, this inequality was proven in [45] (see [45], Section 5). However, even for the most general case Inequality $(28)_2$ holds. A proof is contained in Appendix A. As a consequence, the model predicts a positive dissipation.

4 Numerical implementation

This section contains the numerical implementation of the constitutive model proposed in Section 3. The algorithmic formulation is restricted to the material point level (see [26, 27, 35, 46, 47]). In contrast to previous works [26, 27, 35, 47], the most general framework is presented. Referring to the yield function ϕ and the evolution equations, no special assumption has to be

made. Following the algorithmic formulation proposed in [26], the localization surface $\partial_{\mathrm{s}}\Omega$ may rotate. By this means, locking phenomena are reduced [26]. Without applying a rotating formulation, intersecting cracks have to be taken into account (see e.g. [31]). Numerical methods based on a single fixed crack cannot model the difference between primary and secondary cracks (see [26]).

4.1 Stress update algorithm

Referring to the numerical implementation of constitutive equations, the update of the stresses and of the softening variables $\boldsymbol{q}$ represents the principal part of this section. According to Equations (6), (7) and (18), together with the assumed isotropic damage degradation, the stresses and the internal variables $\boldsymbol{q}$ at time t_{n+1} are obtained as

$$\begin{array}{rcl} \boldsymbol{\sigma}_{n+1} & = & \mathbb{C}_{n+1} : \left(\boldsymbol{\nabla}^{\mathrm{sym}} \bar{\boldsymbol{u}}_{n+1} - \tilde{\boldsymbol{\varepsilon}}^{\mathrm{pl}}_{n+1} \right), \\ \boldsymbol{q}_{n+1} & = & \boldsymbol{q}_{n+1} \left(\boldsymbol{\alpha}(\llbracket \boldsymbol{u} \rrbracket) \right). \end{array} \tag{29}$$

Following standard conventions, a trial state is introduced via

$$\begin{array}{rcl} \boldsymbol{\sigma}^{\mathrm{tr}}_{n+1} & := & \mathbb{C}_{n} : \left(\boldsymbol{\nabla}^{\mathrm{sym}} \bar{\boldsymbol{u}}_{n+1} - \tilde{\boldsymbol{\varepsilon}}^{\mathrm{pl}}_{n} \right) \\ \boldsymbol{q}^{\mathrm{tr}}_{n+1} & := & \boldsymbol{q}(\boldsymbol{\alpha}_n). \end{array} \tag{30}$$

This state is characterized by purely elastic deformations ($\lambda = 0$, e.g. $\llbracket \dot{\boldsymbol{u}} \rrbracket = \boldsymbol{0}$). With Equations (30), the discrete loading condition is given as

$$\phi^{\mathrm{tr}}_{n+1}(\boldsymbol{\sigma}^{\mathrm{tr}}_{n+1}, \boldsymbol{q}^{\mathrm{tr}}_{n+1}) > 0. \tag{31}$$

The proposed implementation is based on the so-called return-mapping algorithm. Consequently, the evolution equations are integrated using a backward EULER integration. Applying this integration scheme to the displacement discontinuity and to the evolution of the internal variables $\boldsymbol{\alpha}$ (see Equations (14)), leads to

$$\begin{array}{rcl} \Delta \llbracket \boldsymbol{u} \rrbracket_{n+1} & = & \Delta\lambda_{n+1} \; \partial_{\boldsymbol{t}} g \big|_{n+1} \\ \Delta \boldsymbol{\alpha}_{n+1} & = & \Delta\lambda_{n+1} \; \partial_{\boldsymbol{q}} h \big|_{n+1}. \end{array} \tag{32}$$

Hence, the evolution of the regularly distributed part of the enhanced strains (see Equation (6)) results in

$$\Delta \tilde{\boldsymbol{\varepsilon}}_{n+1} = \Delta\lambda_{n+1} \; \left(\partial_{\boldsymbol{t}} g \otimes \boldsymbol{\nabla} \varphi \right)^{\mathrm{sym}} \big|_{n+1}. \tag{33}$$

Here and henceforth, the notations $\Delta(\bullet)_{n+1} = (\bullet)_{n+1} - (\bullet)_n$ and $\Delta\lambda_{n+1} = \lambda_{n+1} \; \Delta t_{n+1}$ are used. Combining Equations $(30)_1$ and (33) and applying the identity $\mathbb{D} : \mathbb{C} = \mathbb{I}$ (more precisely, the numerically integrated form of the rate of this equation), Equation $(29)_1$ is rewritten as

$$\boldsymbol{\sigma}_{n+1} = \boldsymbol{\sigma}^{\mathrm{tr}}_{n+1} - \mathbb{C}_n : \left(\partial_{\boldsymbol{t}} g \otimes \boldsymbol{\nabla} \varphi \right)^{\mathrm{sym}} \big|_{n+1} \; \Delta\lambda_{n+1}. \tag{34}$$

Since Equation (34) is formally identical to Equation (45) in [31], the return-mapping algorithm as proposed in [31] can be applied to the presented multiscale model without any modification. For that purpose, the residuals

$$\boldsymbol{R} := \left\{ \begin{array}{c} \boldsymbol{R}^{\tilde{\boldsymbol{\varepsilon}}} \\ \boldsymbol{R}^{\boldsymbol{\alpha}} \end{array} \right\} := \left\{ \begin{array}{ccc} -\tilde{\boldsymbol{\varepsilon}}_{n+1} & +\tilde{\boldsymbol{\varepsilon}}_{n} & +\Delta\tilde{\boldsymbol{\varepsilon}}_{n+1} \\ -\boldsymbol{\alpha}_{n+1} & +\boldsymbol{\alpha}_{n} & +\Delta\boldsymbol{\alpha}_{n+1} \end{array} \right\} \tag{35}$$

are defined and if loading is signaled by $\phi^{\mathrm{tr}}_{n+1} > 0$, the root of the set of the nonlinear equations

$$\boldsymbol{R} = \boldsymbol{0} \quad \wedge \quad \phi_{n+1} = 0 \tag{36}$$

is computed by means of NEWTON's method. For further details, refer to [31, 35] (see also [38, 39]). The algorithmic tangent tensor, i.e.

$$\mathbb{C}^{\mathrm{epd}} := \left.\frac{\mathrm{d}\boldsymbol{\sigma}}{\mathrm{d}\boldsymbol{\nabla}^{\mathrm{sym}}\bar{\boldsymbol{u}}}\right|_{n+1}, \tag{37}$$

is derived in a similar fashion to that presented in [31, 35].

Based on the solution of the return-mapping algorithm, the increment of damage evolution, i.e. $\Delta\overline{\psi^{-1}}$ (see Equation (25)), is computed as

$$\Delta\overline{\psi^{-1}}_{n+1} = \beta \left.\frac{(\partial_{\boldsymbol{t}}\phi\otimes\boldsymbol{N}) : \mathbb{C}_0 : (\Delta[\![\boldsymbol{u}]\!]\otimes\boldsymbol{\nabla}\varphi)}{(\partial_{\boldsymbol{t}}\phi\otimes\boldsymbol{N}) : \boldsymbol{\sigma}}\right|_{n+1}. \tag{38}$$

The updated constitutive tensor $\mathbb{C}$ follows from

$$\mathbb{D}_{n+1} = \mathbb{D}_0 \sum_{t=t_0}^{t=t_{n+1}} \Delta\overline{\psi^{-1}}_t \quad \Rightarrow \quad \mathbb{C}_{n+1} = \mathbb{D}_{n+1}^{-1}. \tag{39}$$

Remark 1: According to [26, 27, 35], for non-constant functions $\boldsymbol{\nabla}\varphi$, the average value, i.e.

$$\overline{\boldsymbol{\nabla}\varphi} = \frac{1}{V^{\mathrm{e}}}\int_{\Omega^{\mathrm{e}}} \boldsymbol{\nabla}\varphi \,\mathrm{d}V, \tag{40}$$

is employed. In Equation (40), V^{e} denotes the volume of the respective finite element.

4.2 Finite element formulation

The finite element formulation is based on the weak form of equilibrium. With $\bar{\boldsymbol{\eta}}$ denoting a continuous test-function, $\boldsymbol{f}$ body forces and $\boldsymbol{t}^*$ prescribed traction vectors acting on the NEUMANN boundary $\Gamma_{\boldsymbol{\sigma}}$, the principal of virtual work is written as

$$\int_{\Omega^e} \boldsymbol{\nabla}^{\mathrm{sym}}\bar{\boldsymbol{\eta}} : \boldsymbol{\sigma} \,\mathrm{d}V = \int_{\Omega^e} \bar{\boldsymbol{\eta}}\cdot\boldsymbol{f} \,\mathrm{d}V + \int_{\Gamma^e_{\boldsymbol{\sigma}}} \bar{\boldsymbol{\eta}}\cdot\boldsymbol{t}^* \,\mathrm{d}\Gamma. \tag{41}$$

Since the discontinuous part of the displacement field, i.e. $[\![\boldsymbol{u}]\!]$, is modeled in an incompatible sense, and is therefore restricted to the element level, e.g. material point level, $\bar{\boldsymbol{u}}$ represents the only global displacement field. Adopting a GALERKIN-type approximation of the continuous displacements, the fields $\bar{\boldsymbol{u}}$ and $\bar{\boldsymbol{\eta}}$ are assumed as

$$\begin{aligned} \bar{\boldsymbol{u}} &\approx \sum_{i=1}^{n_{\mathrm{node}}} N_i\,\bar{\boldsymbol{u}}_i^e \\ \bar{\boldsymbol{\eta}} &= \sum_{i=1}^{n_{\mathrm{node}}} N_i\,\bar{\boldsymbol{\eta}}_i^e \end{aligned} \quad \Rightarrow \quad \begin{aligned} \boldsymbol{\nabla}\bar{\boldsymbol{u}} &\approx \sum_{i=1}^{n_{\mathrm{node}}} \bar{\boldsymbol{u}}_i^e\otimes\boldsymbol{\nabla}N_i \\ \boldsymbol{\nabla}\bar{\boldsymbol{\eta}} &= \sum_{i=1}^{n_{\mathrm{node}}} \bar{\boldsymbol{\eta}}_i^e\otimes\boldsymbol{\nabla}N_i. \end{aligned} \tag{42}$$

In accordance to Equation (3), N_i denotes the standard interpolation function associated with node i. The solution associated with the nonlinear problem described by Equation (41) is computed efficiently using NEWTON's method. Consequently, the linearization of Equation (41) is required. Applying Equation (37), this linearization results in

$$\int_{\Omega^e} \boldsymbol{\nabla}^{\mathrm{sym}}\bar{\boldsymbol{\eta}} : \mathbb{C}^{\mathrm{epd}} : \boldsymbol{\nabla}^{\mathrm{sym}}\Delta\bar{\boldsymbol{u}} \,\mathrm{d}V = \int_{\Omega^e} \bar{\boldsymbol{\eta}}\cdot\Delta\boldsymbol{f} \,\mathrm{d}V + \int_{\Gamma^e_{\boldsymbol{\sigma}}} \bar{\boldsymbol{\eta}}\cdot\Delta\boldsymbol{t}^* \,\mathrm{d}\Gamma. \tag{43}$$

In Equation (43), $\Delta\bar{\boldsymbol{u}}$, $\Delta\boldsymbol{F}$ and $\Delta\boldsymbol{t}^*$ represent the incremental nodal displacements, the increment of the body forces $\boldsymbol{f}$ and the increment of the prescribed NEUMANN boundary conditions, respectively. Note that Equations (41)-(43) are formally identical to standard continuum models (see [38, 39]).

5 Numerical examples

The applicability and performance of the proposed numerical implementation is investigated by means of a three-dimensional ultimate load analysis of a notched concrete beam (Subsection 5.1) as well as by means of a re-analysis of a two-dimensional L-shaped slab (Subsection 5.2). For prognoses of mode-I fracture of brittle materials, the RANKINE yield function characterized by a failure function of the format $\phi = (\boldsymbol{N} \otimes \boldsymbol{N}) : \boldsymbol{\sigma} - q(\alpha)$ is adopted. Applying the rotating formulation [26, 35], the vector $\boldsymbol{N}$ coincides with the direction of the maximum principle stress.

5.1 Notched concrete beam

This subsection contains numerical analyses of a notched concrete beam using the proposed three-dimensional finite element formulation. The geometry, the loading and boundary conditions of the beam and the material parameters are contained in Figure 2. The dimensions as well as the material parameters are chosen according to [44]. For the modeling of the steel

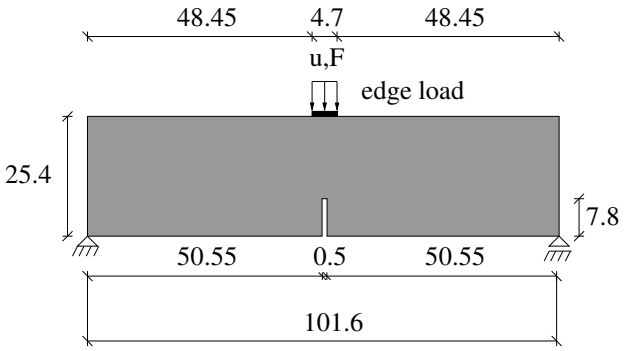

E = $4.36 \cdot 10^3$ [KN/cm^2]
ν = 0.2
f_{tu}= 0.4 [KN/cm^2]
$\mathcal{G}_{\mathrm{f}}$ = $1.195 \cdot 10^{-3}$ [KN cm/cm^2]
β = 0.4

Figure 2: Numerical study of a notched concrete beam: Dimensions (in [cm]) and material parameters; thickness of the beam $t = 12.7$ cm.

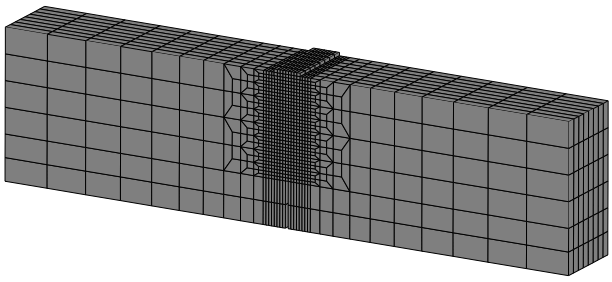

Figure 3: Numerical study of a notched concrete beam: Three-dimensional discretization by means of 6792 tri-linear brick elements.

loading platen, HOOKE's law is adopted ($E = 2.1 \cdot 10^4$ kN/cm^2, $\nu = 0.3$). Frictionless contact

is assumed between the steel platen and the concrete. The softening behavior is governed by the hyperbolic law

$$q(\alpha) = f_{\mathrm{tu}} \, \frac{1}{\left(1 - \frac{\alpha}{\alpha_{\mathrm{u}}}\right)^2}, \quad \text{with} \quad \alpha_{\mathrm{u}} = \frac{\mathcal{G}_{\mathrm{f}}}{\left(1 - \frac{\beta}{2}\right) \, f_{\mathrm{tu}}}, \tag{44}$$

where $\mathcal{G}_{\mathrm{f}}$ denotes the specific fracture energy of concrete in tension and f_{tu} is the uniaxial tensile strength of concrete. The finite element discretization by means of 6792 tri-linear brick elements is illustrated in Figure 3. Convergence is checked according to the relative maximum norm of the residuals with a tolerance set to $tol = 10^{-8}$.

In contrast to References [26, 44], loading on top of the beam was applied by incrementally increasing nodal displacements along only one outer edge of the loading platen. By this, the beam is subjected to bending but also to torsion. Consequently, the ultimate load has to be smaller than its counterpart computed in [26, 44]. Furthermore, the stress states resulting from the torsional loading are fully three-dimensional. Hence, the numerical analyses cannot be reduced, neither to plane strain nor to plane stress conditions.

Figure 4 contains the load-displacement diagram obtained from the proposed elastoplastic isotropic damage model (referred as model "isotropic"). Additionally, the results based on the anisotropic elastoplastic damage model (referred as "anisotropic") published in [35] are illustrated. Both models lead to almost identical results. However, the computational costs associ-

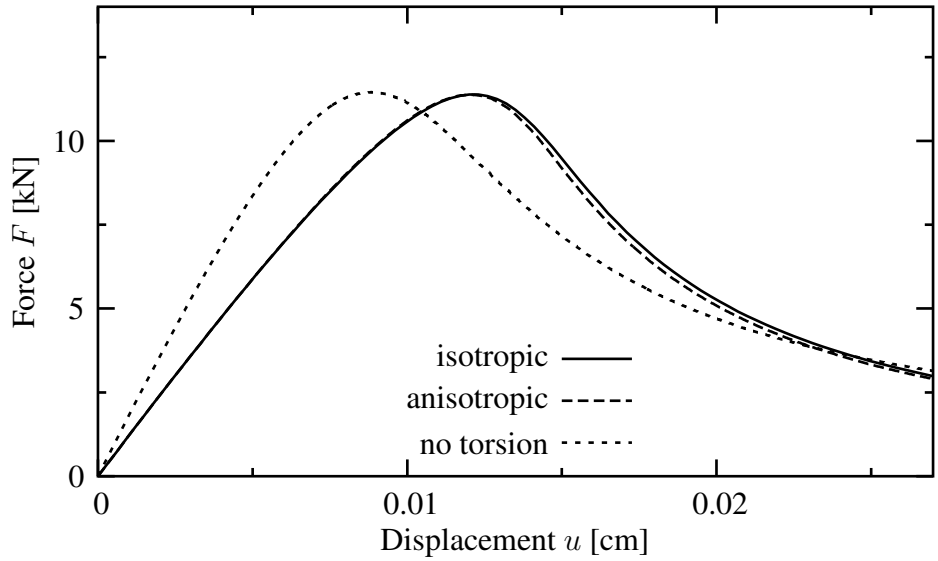

Figure 4: Numerical study of a notched concrete beam: Load-displacement diagrams obtained from the proposed elastoplastic isotropic damage model and the elastoplastic anisotropic damage model as suggested in [35].

ated with the isotropic damage model decrease significantly compared to those corresponding to the anisotropic counterpart. For a better interpretation of the computed results, the analysis is repeated with a uniformly distributed surface loading acting on the loading platen. Hence, torsional effects are eliminated. The respective load-displacement diagram (referred as "no torsion") is illustrated in Figure 4. As anticipated, the structural response associated with this load case becomes stiffer. However, the ultimate loads corresponding to both different loadings are almost identical. The reason for this surprising result will be given in the following paragraph.

Figure 5 contains the distribution of the internal variable $\alpha = \int_T [\![\dot{\boldsymbol{u}}]\!] \cdot \boldsymbol{N} \, \mathrm{d}t$ representing an equivalent crack width at a cutting plane across the symmetry axis of the beam for different load stages. According to Figure 5, the proposed elastoplastic isotropic damage model predicts crack

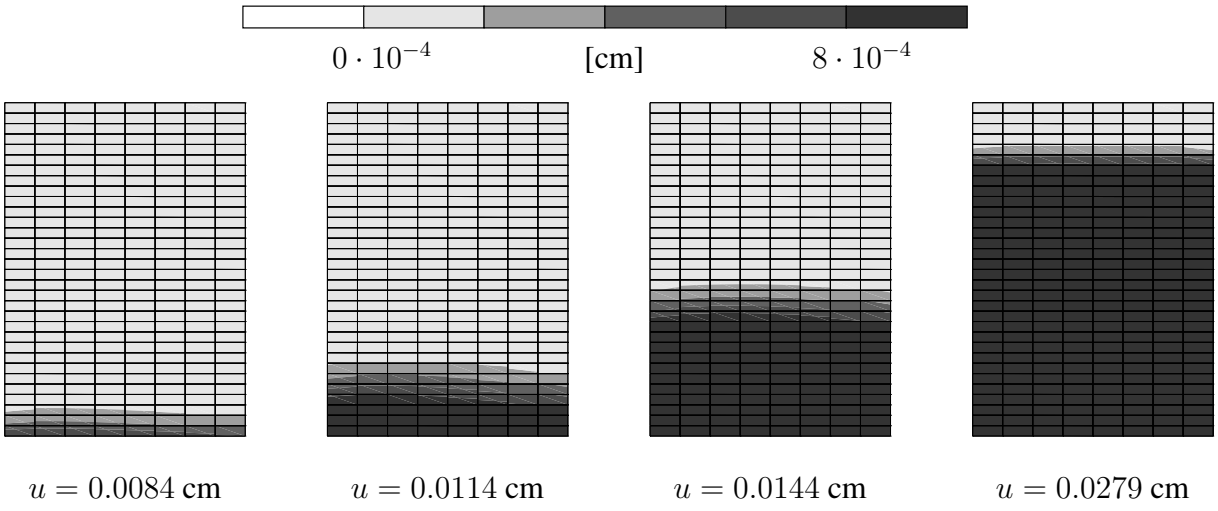

Figure 5: Numerical study of a notched concrete beam: Distribution of the internal variable α representing the crack width obtained from the proposed elastoplastic isotropic damage model.

initiation at the notch opposite to the side where the edge load was applied. In contrast to the numerical analysis of the notched beam presented in [44, 45], the prescribed edge load results in torsional moments and, consequently, in a non-symmetrical distribution of the internal variable α (see state $u = 0.0084$ cm and $u = 0.0114$ cm). However, at a later stage of deformation ($u = 0.0144$ cm), the influence of torsion becomes weaker. The final failure mechanism ($u = 0.0279$ cm) is characterized by an almost symmetrical distribution of the internal variable and is nearly identical to that corresponding to the load case of a uniformly distributed surface load acting on the loading platen as analyzed in [44, 45]. Hence, the ultimate loads associated with both load cases differ only marginally.

Figure 6 contains the distribution of the internal variable $\alpha = \int_T [\![\dot{\boldsymbol{u}}]\!] \cdot \boldsymbol{N} \, \mathrm{d}t$ obtained from the elastoplastic anisotropic damage model [35] at a cutting plane across the symmetry axis of the beam for different load stages. From comparing Figure 6 and Figure 5 it is concluded that both finite element formulations lead to almost identical results. As mentioned, the proposed elastoplastic isotropic damage model strongly reduces the computational costs with negligible loss of accuracy.

5.2 L-shaped slab

This subsection is concerned with a re-analysis of an L-shaped slab [27, 35, 48]. The geometry and material parameters of the problem are illustrated in Figure 7. According to Equation (44), a hyperbolic softening evolution is assumed. The displacement controlled analysis is performed by means of 6 different discretizations (see Figure 8). Mesh I, II, III, IV, V and mesh VI contains 48, 114, 261, 642, 1779 and 5580 bi-linear plane stress elements, respectively. Loading is applied by prescribing vertical displacements at all nodes along the right edge of the slab. Convergence is checked according to the criterion

$$\frac{||\boldsymbol{r}_i - \boldsymbol{r}_e||_\infty}{||\boldsymbol{r}_e||_\infty} < tol \tag{45}$$

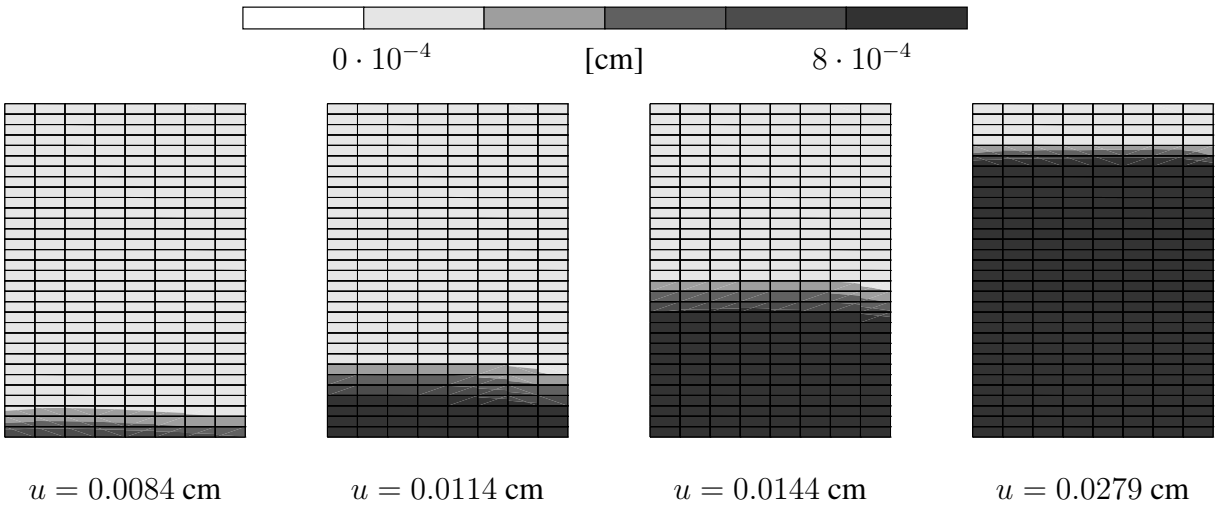

Figure 6: Numerical study of a notched concrete beam: Distribution of the internal variable α representing the crack width obtained from the elastoplastic anisotropic damage mode as suggested in [35].

based on the maximum norm $|| \bullet ||_\infty$, where $\boldsymbol{r}_i$ ($\boldsymbol{r}_e$) is the vector of internal (external) forces. For the numerical analyses of the L-shaped slab, tolerance is set to $tol = 10^{-8}$.

Figure 9 shows the load-displacement diagram obtained from the presented elastoplastic isotropic damage model for each of the 6 different discretizations. In the post-peak regime, two unloading and reloading cycles have been included. The computed diagrams illustrate the capability of the model to capture fracture-induced stiffness degradation as well as permanent deformations after crack initiation. According to Figure 9, all discretizations predict an almost identical structural response.

Damage accumulation, characterized by the internal variable α, is illustrated in Figure 10. It refers to the final state of the loading process. While discretizations mesh I–III predict a straight localization surface, a slightly curved crack band is observed for finite element meshes IV–VI. The finer the discretization, the more pronounced is this effect.

For a comparison, a re-analysis of the L-shaped slab based on the elastoplastic anisotropic damage model as proposed in [35] is performed. The unchanged material parameters as well as the dimensions of the structure are given in Figure 7. Figure 11 illustrates the computed load-displacement diagrams for the 6 different discretizations (see Figure 8). By comparison between Figure 11 and Figure 9 it is concluded that the numerical results obtained from the anisotropic damage model depend on the spatial discretization more strongly than their counterparts computed from the isotropic formulation.

The distribution of the internal variable α representing an equivalent crack width as predicted from the anisotropic elastoplastic damage model is shown in Figure 12. Similarly to Figure 10, a straight crack line is obtained from the analyses based on mesh I up to mesh III. With increasing number of finite elements (mesh IV–mesh VI), the shape of the localization surface deviate from a (straight) line. In accordance with the isotropic damage model (see Figure 10), the curvature of the failure zone depends proportionally on the resolution of the spatial discretization (see Figure 12).

Although the crack paths computed from both models are almost identical (compare Figure 12 with Figure 10), the corresponding load-displacement diagrams differ. In contrast to the isotropic damage model, the anisotropic counterpart shows a dependence of the ultimate load

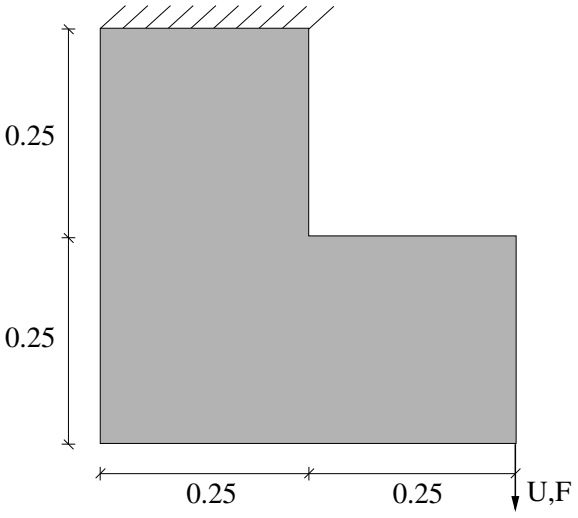

material parameters:

$\mathrm{E} = 2.585{\cdot}10^{3}$ kN/cm^2
$\nu = 0.2$
$f_{\mathrm{tu}} = 2.7{\cdot}10^{-1}$ kN/cm^2
$\mathcal{G}_{\mathrm{f}} = 9.0{\cdot}10^{-4}$ kN/cm
$\beta = 0.4$

Figure 7: 2D finite element analysis of an L-shaped slab: Geometry (dimensions in [m]) and material parameters (thickness of the slab=0.1 m)

on the spatial discretization. However, the same effect is observed also if damage accumulation is neglected, i.e. $\beta = 0$. This has been pointed out in [27, 49] (see also [48]). The reason for this is that the L-shaped slab is characterized by a strong influence of the topology of the crack surface on the structural response (i.e. the load-displacement diagram) [27, 48]. This dependence is reflected in Figure 12 and Figure 11, respectively. As a consequence, the question arises why the numerically computed load-displacement diagrams associated with the isotropic damage model are nearly invariant with respect to the considered finite element mesh.

In order to be able to give an answer to this question, the load-displacement diagrams (Figure 9) as well as the distributions of the internal variable α (Figure 10) as obtained from the new model are re-analyzed. Restricting damage degradation to isotropy, the influence of the orientation of the cracks becomes less significant. More precisely, if a crack has opened, the resulting softening effect is independent of its respective direction. Hence and in contrast to anisotropic damage theories, the most important parameter of the crack topology affecting the structural response is the crack length. According to Figure 10, this length, abbreviated as l_{cr}, associated with the different spatial discretizations is almost identical for each of the finite element meshes (mesh I: $l_{\mathrm{cr}} \approx 0.250$ m, mesh VI: $l_{\mathrm{cr}} \approx 0.253$ m). Clearly, the numerical analyses are based on a coupling parameter $\beta = 0.4$ and not on purely damage-induced stiffness degradation ($\beta = 1.0$). Consequently, it has to be shown that the numerically computed results obtained from the coupled elastoplastic damage model setting $\beta = 0.4$ are almost identical to those of the pure damage theory. For that purpose, a re-analysis setting $\beta = 1.0$ is performed. From Figure 13 the good agreement between the coupled ($\beta = 0.4$) and the pure damage model ($\beta = 1.0$) can be observed. The small differences between the structural response computed result from the fact that β slightly influences the shape of the load-displacement diagram, see Remark 2. However, the fracture energy does not depend on β, cf. [35, 44].

Remark 2: $\beta = 0.4$ does not mean that 40% of the inelastic strains correspond to plastic strains and 60% to damage-induced strains. According to [44], an exponential softening evolution $q(\alpha)$ results in an exponential stress-strain relationship for $\beta = 0$. However, for $\beta = 1.0$ a linear stress-strain law is obtained. Consequently, the influence of β on the decomposition of the inelastic strains is nonlinear.

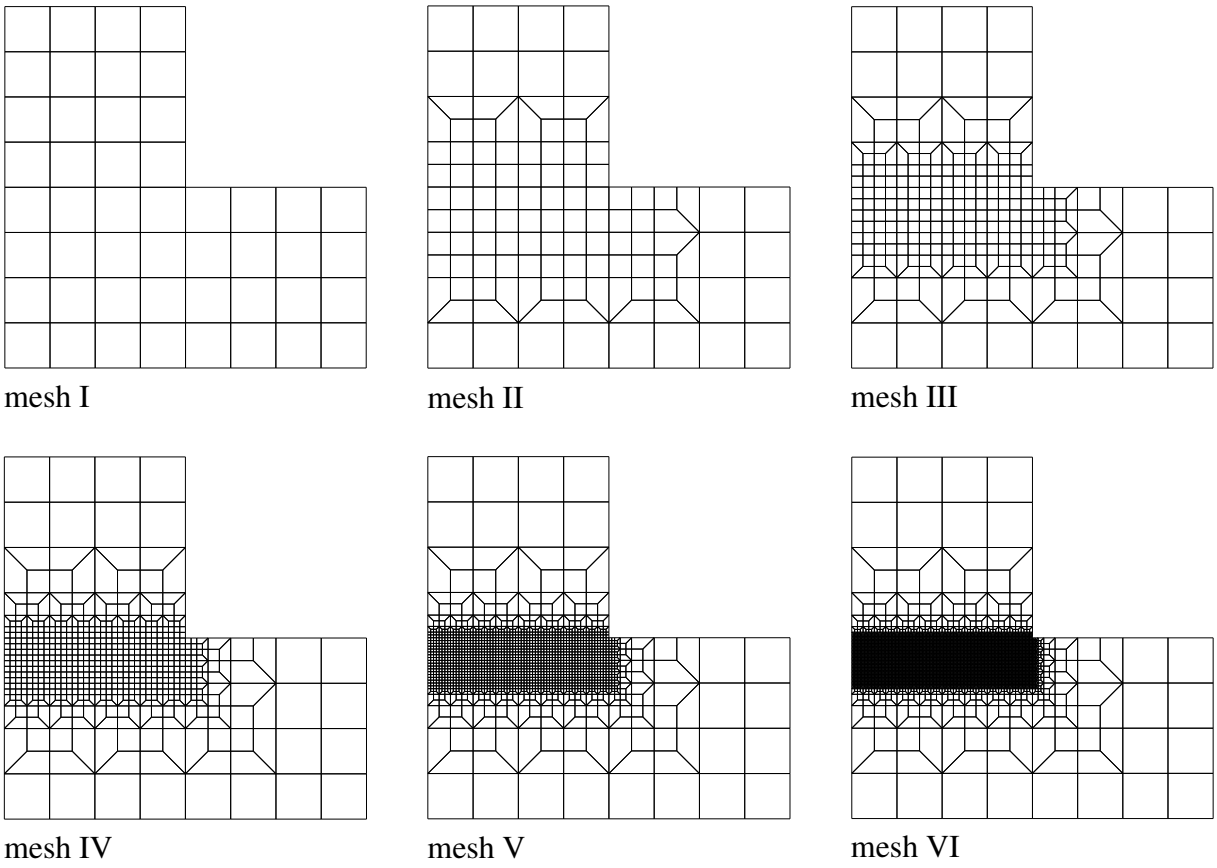

Figure 8: 2D finite element analysis of an L-shaped slab: Finite element discretizations containing 48, 114, 261, 642, 1779 and 5580 bi-linear plane stress elements.

6 Conclusion

A multiscale finite element formulation suitable for the analysis of large-scale engineering structures has been presented in this paper. The proposed traction-separation law governing the inelastic material response is based on an elastoplastic isotropic damage model. In contrast to previous works, the suggested framework covers a broad range of applications including mode-I, mode-II and mixed-mode material failure. Referring to the yield function and the evolution equations, no special assumption has to be made. The developed interface law has been incorporated within a 4-node plane stress element and an 8-node brick element.

Based on a recently proposed algorithmic framework [26, 27, 35, 45], the integration of the constitutive equations results in a format suitable for the application of the standard return-mapping algorithm [38]. Only minor modifications of the by now classical material routines designed for standard plasticity models are required.

The applicability and the performance of the proposed finite element formulation is investigated by means of a three-dimensional ultimate load analysis of a notched concrete beam subjected to an eccentric load as well as by means of a re-analysis of a two-dimensional L-shaped slab. The robustness of the suggested finite element implementation is documented by the analysis of the notched concrete beam. By comparing the computed results with those obtained from an elastoplastic anisotropic damage model it is concluded that the new finite element formulation reduces computational cost strongly with negligible loss of accuracy. The analysis of the L-shaped slab pointed out the difference between an isotropic and an anisotropic

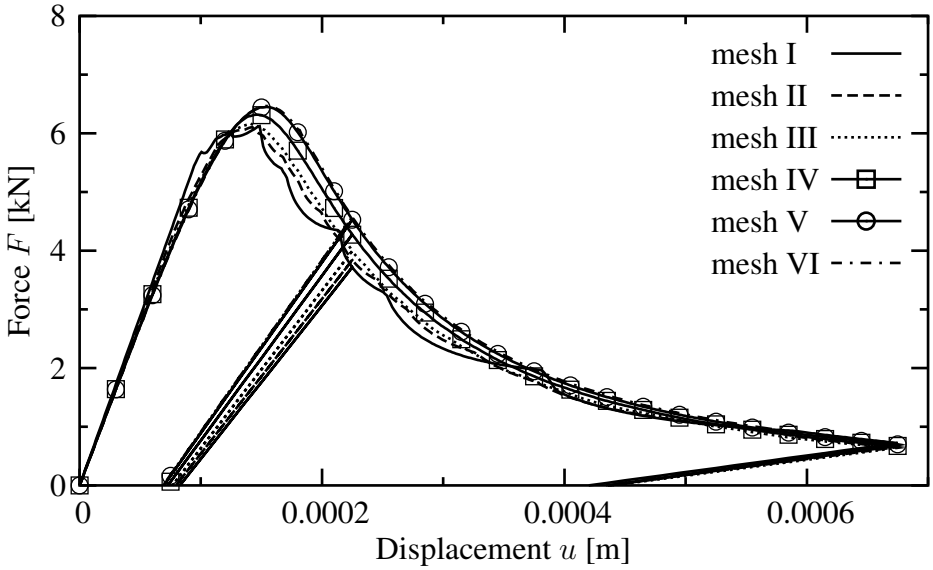

Figure 9: 2D finite element analysis of an L-shaped slab: Load-displacement diagram obtained from the proposed elastoplastic isotropic damage model for 6 different discretizations (see Figure 8); material parameters according to Figure 7.

degradation of the stiffness.

Acknowledgement

This work was completed under the financial support of the Deutsche Forschungsgemeinschaft (DFG) through project A4 under supervision of Prof. O.T. Bruhns within the Collaborative Research Centre 398. The author wishes to express his sincere gratitude to this support. Furthermore, the author would like to thank Prof. O.T. Bruhns for his helpful comments.

A Proof of Inequality (28)

In this paragraph, we present a proof of

$$\overset{\cdot}{\overline{\psi^{-1}}} \geq 0 \quad \Longleftrightarrow \quad (\boldsymbol{N} \otimes \boldsymbol{m}) : \mathbb{C}_0 : (\boldsymbol{m} \otimes \boldsymbol{\nabla}\varphi) \geq 0. \tag{46}$$

for the most general case. According to Inequality $(46)_2$, the variables involved in this proof are the three vectors $\boldsymbol{N}$, $\boldsymbol{m}$ and $\boldsymbol{\nabla}\varphi$. For these three vectors some physical restrictions have to be accounted for. At first, we know that $\boldsymbol{N} \cdot \boldsymbol{\nabla}\varphi \geq 0$. This inequality follows from the physical interpretation of this scalar product as a numerical length scale (see [45, 50]). Secondly, the inequality $\boldsymbol{N} \cdot \boldsymbol{m} \geq 0$ has to be fulfilled. This restriction is equivalent to the local impenetrability condition of continuum mechanics. Furthermore and without loss of generality, we set $\boldsymbol{N} = \boldsymbol{e}_1$, i.e. $\boldsymbol{N}$ is equal to the first base vector of a CARTESIAN coordinate system defined by the triad ($\boldsymbol{e}_1$, $\boldsymbol{e}_2$, $\boldsymbol{e}_3$). Since Inequality $(46)_2$ is linear in $\boldsymbol{\nabla}\varphi$, we are allowed to postulate $\boldsymbol{\nabla}\varphi$ as a unit vector, i.e. $\boldsymbol{\nabla}\varphi \in \mathcal{S}^2$ (the 2-sphere). Additionally, Inequality $(46)_2$ represents a smooth mapping (with respect to $\boldsymbol{m}$ and $\boldsymbol{\nabla}\varphi$, resp. the components). Combining this smoothness with the fact that the set of all admissible vectors $\boldsymbol{m}, \boldsymbol{\nabla}\varphi \in \mathcal{S}^2$ is compact, we know that the mapping $(46)_2$ attains its minimum on this set.

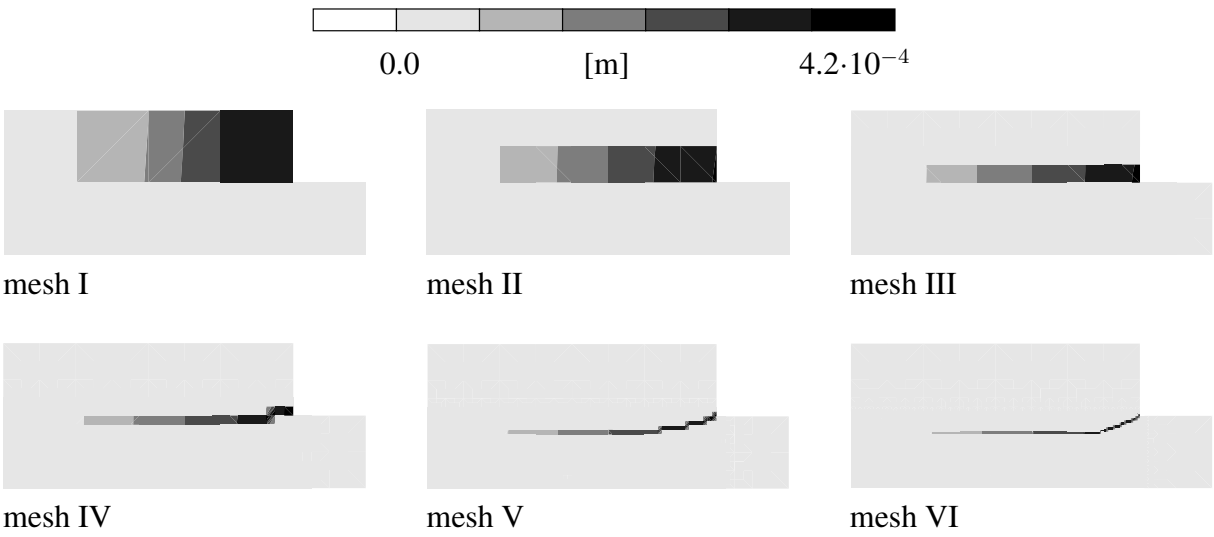

Figure 10: 2D finite element analysis of an L-shaped slab: Distribution of the internal variable α obtained from the proposed elastoplastic isotropic damage model for 6 different discretizations (see Figure 8); material parameters according to Figure 7.

Since the proof becomes lengthy in 3D, attention is restricted to plane stress conditions. However, the proof in 3D follows identical lines. At first, we derive the extremum condition necessary for a local minimum. With

$$\mathbb{C}_0 = \frac{E}{1+\nu}\mathbb{I}^{\mathrm{sym}} + \frac{E\,\nu}{1-\nu^2}\,\mathbf{1}\otimes\mathbf{1}, \tag{47}$$

we obtain

$$\begin{aligned} f := (\boldsymbol{N}\otimes\boldsymbol{m}) : \mathbb{C}_0 : (\boldsymbol{m}\otimes\boldsymbol{\nabla}\varphi) = &\frac{1}{2}\frac{E}{1+\nu}\;[(\boldsymbol{N}\cdot\boldsymbol{m})(\boldsymbol{m}\cdot\boldsymbol{\nabla}\varphi) + \boldsymbol{N}\cdot\boldsymbol{\nabla}\varphi] \\ &+\frac{E\,\nu}{1-\nu^2}\;(\boldsymbol{N}\cdot\boldsymbol{m})(\boldsymbol{m}\cdot\boldsymbol{\nabla}\varphi). \end{aligned} \tag{48}$$

In Equation (47), $\mathbb{I}^{\mathrm{sym}}$ denotes the symmetric fourth-oder unit tensor characterized by $\mathbb{I}^{\mathrm{sym}} : \boldsymbol{A} = \boldsymbol{A}^{\mathrm{sym}}$ for all second-order tensors $\boldsymbol{A}$. Inserting $\boldsymbol{N} = \boldsymbol{e}_1$ (i.e. $\boldsymbol{N}^T = [1;0]$) into Equation (48), together with the description of the unknown vectors $\boldsymbol{m}$ and $\boldsymbol{\nabla}\varphi$ in terms of polar coordinates, i.e.

$$\boldsymbol{N}^T = [1;0], \quad \boldsymbol{m}^T = [\cos\alpha;\sin\alpha] \quad \text{and} \quad \boldsymbol{\nabla}\varphi^T = [\cos\theta;\sin\theta], \tag{49}$$

with $\theta, \alpha \in [-90°; 90°]$ (alternatively, in 3D spherical coordinated have to be used), the first extremum condition reads

$$\frac{\partial f}{\partial \alpha} = \frac{E}{2\,(\nu-1)}\;\sin[2\alpha-\theta] = 0. \tag{50}$$

Hence, the restriction $2\alpha = \theta$ must hold. Computing the second extremum condition, together with $2\alpha = \theta$, yields

$$\frac{\partial f}{\partial \theta} = \frac{E\,(3-\nu)}{4\,(\nu^2-1)}\;\sin\theta = 0. \tag{51}$$

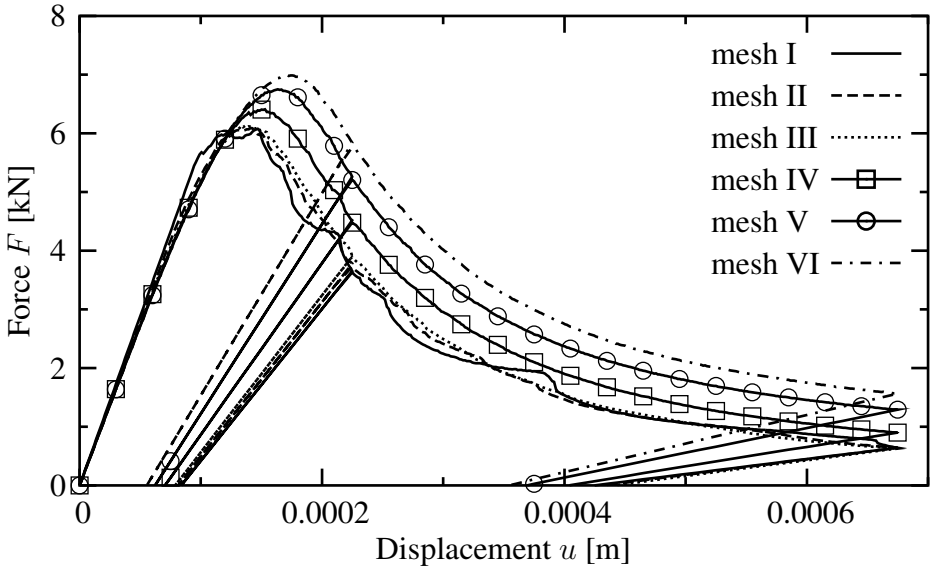

Figure 11: 2D finite element analysis of an L-shaped slab: Load-displacement diagram obtained from the elastoplastic anisotropic damage model [35] for 6 different discretizations (see Figure 8); material according to Figure 7.

Consequently, the solution $\alpha = \theta = 0^\circ$ represents the only possible extremum in the interior of the set $[-90^\circ; 90^\circ] \times [-90^\circ; 90^\circ]$. However, it can be shown easily that this point is associated with a maximum. Thus, the minimum is attained at the boundary of the set $[-90^\circ; 90^\circ] \times [-90^\circ; 90^\circ]$. Looking for the minimum of the mapping f at the boundary of $[-90^\circ; 90^\circ] \times [-90^\circ; 90^\circ]$ in a similar fashion, the global minimum is computed as

$$\min_{\alpha,\theta} f = \frac{E}{2\sqrt{2}\,(1+\nu)} > 0, \quad \text{with} \quad (\alpha, \theta) \in [-90^\circ; 90^\circ] \times [-90^\circ; 90^\circ]. \tag{52}$$

This completes the proof. As mentioned before, the same procedure can also be applied to prove Inequality (46) in 3D.

References

[1] T. Belytschko, J. Fish, and B.E. Engelmann. A finite element with embedded localization zones. *Computer Methods in Applied Mechanics and Engineering*, 70:59–89, 1988.

[2] J. Hadamard. Leçons sur la Propagation des Ondes. *Librairie Scientifique A. Hermann et Fils, Paris*, 1903.

[3] J.E. Marsden and T.J.R. Hughes. *Mathematical foundation of elasticity*. Dover, New York, 1994.

[4] R. De Borst. *Non-linear analysis of frictional materials*. PhD thesis, Technical University Delft, 1986.

[5] R. De Borst. Some recent issues in computational mechanics. *International Journal for Numerical Methods in Engineering*, 52:63–95, 2001.

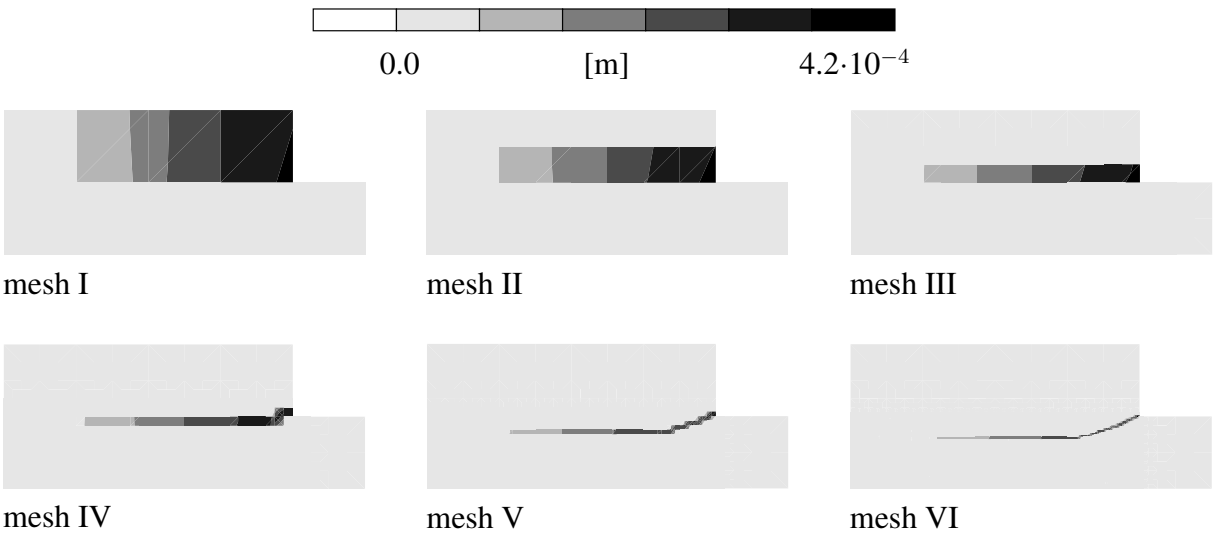

Figure 12: 2D finite element analysis of an L-shaped slab: Distribution of the internal variable α obtained from the elastoplastic anisotropic damage model [35] for 6 different discretizations (see Figure 8); material according to Figure 7.

[6] G. Pijaudier-Cabot and Z.P. Bažant. Nonlocal damage theory. *Journal of Engineering Mechanics (ASCE)*, 113:1512–1533, 1987.

[7] Z.P. Bažant and G. Pijaudier-Cabot. Nonlocal damage, localization, instability and convergence. *Journal of Applied Mechanics*, 55:287–293, 1988.

[8] H.B. Mühlhaus and E.C. Aifantis. A variational principle for gradient plasticity. *International Journal for Solids and Structures*, 28:845–857, 1991.

[9] R. De Borst and H.B. Mühlhaus. Gradient-dependent plasticity: Formulation and algorithmic aspects. *International Journal for Numerical Methods in Engineering*, 35:521–539, 1992.

[10] R. De Borst. Simulation of strain localization: A reappraisal of the cosserat continuum. *Engineering Computations*, 8:317–332, 1991.

[11] P. Steinmann and K.J. Willam. Localization within the framework of micropolar elastoplasticity. In V. Mannl, J. Najar, and O. Brüller, editors, *Advances in continuum mechanics*, pages 296–313. Springer, Berlin-Heidelberg, 1991.

[12] Y.W. Chang and R.J. Asaro. An experimental study of shear localization in aluminium-copper single crystals. *Acta Metallurgica and Materials*, 29:241–257, 1981.

[13] T.B. Cox and J.R. Low Jr. An investigation of the plastic fracture of AISI 4340 and 18 Nickel-200 grade maraging steels. *Metallurgical and Materials Transactions*, 5:1457–1470, 1974.

[14] J. Simo, J. Oliver, and F. Armero. An analysis of strong discontinuities induced by strain softening in rate-independent inelastic solids. *Computational Mechanics*, 12:277–296, 1993.

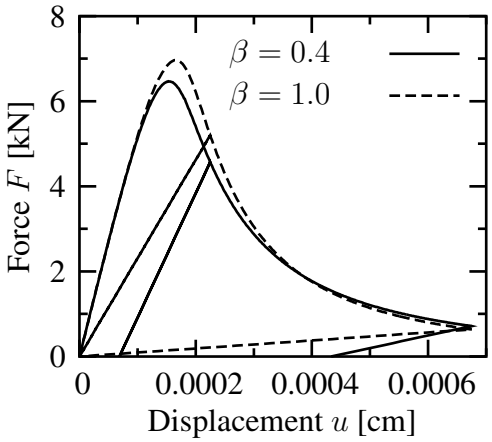

Figure 13: 2D finite element analysis of an L-shaped slab: Comparison of load-displacement diagrams obtained from the proposed elastoplastic isotropic damage model based on mesh VI: $\beta = 0.4$ vs. $\beta = 1.0$ (purely damage theory)

[15] K. Garikipati and T.J.R. Hughes. A study of strain localization in a multiple scale framework - the one-dimensional problem. *Computer Methods in Applied Mechanics and Engineering*, 159(3-4):193–222, 1998.

[16] F. Armero. Large-scale modeling of localized dissipative mechanisms in a local continuum: applications to the numerical simulation of strain localization in rate-dependent inelastic solids. *Mechanics of Cohesive-Frictional Materials*, 4:101–131, 1999.

[17] R.I. Borja. Finite element simulation of strain localization with large deformation: capturing strong discontinuity using a Petrov-Galerkin multiscale formulation. *Computer Methods in Applied Mechanics and Engineering*, 191:2949–2978, 2002.

[18] N. Moës, J. Dolbow, and T. Belytschko. A finite element method for crack growth without remeshing. *International Journal for Numerical Methods in Engineering*, 46:131–150, 1999.

[19] K. Garikipati. Variational multiscale methods to embed the macromechanical continuum formulation with fine-scale strain gradient theories. *International Journal for Numerical Methods in Engineering*, 57:1283–1298, 2003.

[20] M. Ortiz and E.A. Repetto. Nonconvex energy minimisation and dislocation in ductile single crystals. *Journal of the Mechanics and Physics of Solids*, 47:397–462, 1999.

[21] C. Carstensen, K. Hackl, and A. Mielke. Non-convex potentials and microstructures in finite-strain plasticity. *Proceedings of the Royal Society of Lond, Series A*, 458:299–317, 2002.

[22] C. Miehe and M. Lambrecht. Analysis of microstructures development in shearbands by energy relaxation of incremental stress potentials: Large-strain theory for standard dissipative solids. *International Journal for Numerical Methods in Engineering*, 58:1–41, 2003.

[23] J. Oliver and J. Simo. Modelling strong discontinuities in solid mechanics by means of strain softening constitutive equations. In H. Mang, N. Bićanić, and R. de Borst, editors, *Computational Modelling of concrete structures*, pages 363–372. Pineridge press, 1994.

[24] J. Simo and J. Oliver. A new approach to the analysis and simulation of strain softening in solids. In Z.P. Bažant, Z. Bittnar, M. Jirásek, and J. Mazars, editors, *Fracture and Damage in Quasibrittle Structures*, pages 25–39. E. &F.N. Spon, London, 1994.

[25] J. Oliver. Modelling strong discontinuities in solid mechanics via strain softening constitutive equations part 1: Fundamentals. part 2: Numerical simulations. *International Journal for Numerical Methods in Engineering*, 39:3575–3623, 1996.

[26] J. Mosler and G. Meschke. 3D modeling of strong discontinuities in elastoplastic solids: Fixed and rotating localization formulations. *International Journal for Numerical Methods in Engineering*, 57:1553–1576, 2003.

[27] J. Mosler. *Finite Elemente mit sprungstetigen Abbildungen des Verschiebungsfeldes für numerische Analysen lokalisierter Versagenszustände in Tragwerken*. PhD thesis, Ruhr Universität Bochum, 2002.

[28] M. Klisinski, K. Runesson, and S.. Sture. Finite element with inner softening band. *Journal of Engineering Mechanics (ASCE)*, 117(3):575–587, 1991.

[29] T. Olofsson, M. Klisinski, and P. Nedar. Inner softening bands: A new approach to localization in finite elements. In H. Mang, N. Bićanić, and R. de Borst, editors, *Computational Modelling of Concrete Struct.*, pages 373–382. Pineridge press, 1994.

[30] U. Ohlsson and T. Olofsson. Mixed-mode fracture and anchor bolts in concrete: Analysis with inner softening bands. *Journal of Engineering Mechanics (ASCE)*, 123:1027–1033, 1997.

[31] J. Mosler. On the modeling of highly localized deformations induced by material failure: The strong discontinuity approach. *Archives of Computational Methods in Engineering*, 2004. submitted.

[32] F. Armero and K. Garikipati. An analysis of strong discontinuities in multiplicative finite strain plasticity and their relation with the numerical simulation of strain localization in solids. *International Journal for Solids and Structures*, 33:2863–2885, 1996.

[33] A.R. Regueiro and R.I. Borja. A finite element method of localized deformation in frictional materials taking a strong discontinuity approach. *Finite Elements in Analysis and Design*, 33:283–315, 1999.

[34] F. Armero. Localized anisotropic damage of brittle materials. In D.R.J. Owen, E. Oñate, and E. Hinton, editors, *Computational Plasticity*, volume 1, pages 635–640, 1997.

[35] J. Mosler and O.T. Bruhns. A 3D anisotropic elastoplastic-damage model using discontinuous displacement fields. *International Journal for Numerical Methods in Engineering*, 60:923–948, 2003.

[36] M. Ortiz. A constitutive theory for the inelastic behavior of concrete. *Mechanics of Materials*, 4:67–93, 1985.

[37] S. Govindjee, G.J. Kay, and J.C. Simo. Anisotropic modeling and numerical simulation of brittle damage in concrete. *International Journal for Numerical Methods in Engineering*, 38, 1995.

[38] J. Simo and T.J.R. Hughes. *Computational inelasticity*. Springer, New York, 1998.

[39] J.C. Simo. Numerical analysis of classical plasticity. In P.G. Ciarlet and J.J. Lions, editors, *Handbook for numerical analysis*, volume IV. Elsevier, Amsterdam, 1998.

[40] H. Matthies, G. Strang, and E. Christiansen. The saddle point of a differential program. In Glowinski, Robin, and Zienkiewicz, editors, *Energy methods in finite element analysis*, pages 309–318. J. Wiley and sons: London, 1979.

[41] R. Teman and G. Strang. Functions of bounded deformations. *Archive for Rational Mechanics ans Analysis*, 75:7–21, 1980.

[42] I. Stakgold. *Green's functions and boundary value problems*. Wiley, 1998.

[43] J.C. Simo and S. Rifai. A class mixed assumed strain methods and the method of incompatible modes. *International Journal for Numerical Methods in Engineering*, 29:1595–1638, 1990.

[44] G. Meschke, R. Lackner, and H.A. Mang. An anisotropic elastoplastic-damage model for plain concrete. *International Journal for Numerical Methods in Engineering*, 42:703–727, 1998.

[45] J. Mosler and G. Meschke. Embedded cracks vs. smeared crack models: a comparison of elementwise discontinuous crack path approaches with emphasis on mesh bias. *Computer Methods in Applied Mechanics and Engineering*, 193:3351–3375, 2004.

[46] R.I. Borja. A finite element model for strain localization analysis of strongly discontinuous fields based on standard galerkin approximation. *Computer Methods in Applied Mechanics and Engineering*, 190:1529–1549, 2000.

[47] J. Mosler and G. Meschke. FE-modeling of displacement discontinuities in inelastic continua. *Zeitschrift für Angewandte Mathematik und Mechanik*, 81(Suppl. 4):875–876, 2001.

[48] B. Winkler. *Traglastuntersuchungen von unbewehrten und bewehrten Betonstrukturen auf der Grundlage eines objektiven Werkstoffgesetzes für Beton*. PhD thesis, Universität Insbruck, 2001.

[49] J. Mosler and G. Meschke. Analysis of mode I failure in brittle materials using the strong discontinuity approach with higher order elements. In *2. European Congress on Computational Mechanics*, 2001.

[50] J. Oliver. A consistent characteristic length for smeared cracking models. *International Journal for Numerical Methods in Engineering*, 28:461–474, 1989.